

Real-Time FEM-Based Registration of 3-D to 2.5-D Transrectal Ultrasound Images

Golnoosh Samei¹, Orcun Goksel, Julio Lobo, Omid Mohareri, Peter Black, Robert Rohling, and Septimiu Salcudean

Abstract—We present a novel technique for real-time deformable registration of 3-D to 2.5-D transrectal ultrasound (TRUS) images for image-guided, robot-assisted laparoscopic radical prostatectomy (RALRP). For RALRP, a pre-operatively acquired 3-D TRUS image is registered to thin-volumes comprised of consecutive intra-operative 2-D TRUS images, where the optimal transformation is found using a gradient descent method based on analytical first and second order derivatives. Our method relies on an efficient algorithm for real-time extraction of arbitrary slices from a 3-D image deformed given a discrete mesh representation. We also propose and demonstrate an evaluation method that generates simulated models and images for RALRP by modeling tissue deformation through patient-specific finite-element models (FEM). We evaluated our method on *in-vivo* data from 11 patients collected during RALRP and focal therapy interventions. In the presence of an average landmark deformation of 3.89 and 4.62 mm, we achieved accuracies of 1.15 and 0.72 mm, respectively, on the synthetic and *in-vivo* data sets, with an average registration computation time of 264 ms, using MATLAB on a conventional PC. The results show that the real-time tracking of the prostate motion and deformation is feasible, enabling a real-time augmented reality-based guidance system for RALRP.

Index Terms—Motion compensation, prostatectomy, image registration.

I. INTRODUCTION

RADICAL prostatectomy (RP), the surgical removal of the prostate gland, is a standard treatment of organ-confined prostate cancer. The primary goal of the surgery is to remove the entire prostate and in particular all cancerous tissue (oncological success), while sparing critical structures to preserve

continence and potency (functional success). The difficulty of RP lies in this delicate trade-off between conflicting goals: removing all the cancer, yet sparing critical structures. A major barrier to better RP outcomes is the inability of surgeons to visualize prostate cancer intra-operatively. Augmented reality (AR) has the potential to provide this much-needed visualization, which could be achieved by registering pre-operative magnetic resonance images (MRIs) annotated with regions of high cancer probability, to real-time, intra-operative transrectal ultrasound (TRUS), which could be acquired during RP. This approach of fusing MRI with TRUS is already practiced successfully for prostate biopsy, with several systems in use (e.g. Artemis, Eigen [1]; UroNav, *In Vivo* Corp./Philips Healthcare [2]; and Urostation, Koelis [3]).

TRUS is the medical imaging modality of choice to guide prostate interventions, as TRUS is real-time, easily accessible and the TRUS transducer can be placed proximal to the prostate [4]. TRUS can image the prostate but cannot accurately image prostate cancer. MRI achieves the most accurate prostate cancer imaging [5], however, it cannot be used during RP with existing techniques due to magnetic safety, interference, and limited space. Instead we envision an AR system that displays real-time TRUS images of the prostate, as well as pre-operative MR images, registered to real-time 2D TRUS, that accurately localize the cancer. Such a system has the potential to improve the outcomes of RP by providing the surgeon with real-time image-guidance tools that can accurately show the prostate anatomy and the prostate cancer location, extent, and proximity to critical structures.

We propose to register MRI to TRUS in a two-step process. In the first step, a reference 3D TRUS image of the prostate will be acquired at the start of the surgery. The MRI, which is typically taken days or weeks before the RALRP surgery, needs to be registered to this reference TRUS image. The prostate in TRUS might have undergone deformations due to differences in bladder filling, patient positioning between MR and TRUS acquisitions and the pressure applied to the gland by the ultrasound transducer. Therefore, for the registration of the two volumes a deformable method is required. This is typically achieved by either surface-based [6]–[8] or feature-based [9], [10] methods. We use a surface-based method with a finite element method (FEM) based deformation model, similarly to [6]. In the second step during the surgery, multiple dense 2D TRUS images (hereafter called the '2.5D' volume) are acquired, to which the reference 3D TRUS is

Manuscript received December 21, 2017; revised February 20, 2018; accepted February 24, 2018. Date of publication February 28, 2018; date of current version July 31, 2018. This work was supported by the Canadian Institutes of Health Research and in part by the Charles Laszlo Chair in biomedical engineering held by Prof. Salcudean. (Corresponding author: Golnoosh Samei.)

G. Samei is with the Department of Electrical and Computer Engineering, Robotics and Control Laboratory, Vancouver, BC V6T 1Z4, Canada (e-mail: sameig@ece.ubc.ca)

O. Goksel is with the Department of Information Technology and Electrical Engineering, ETH Zürich, 8092 Zürich, Switzerland.

J. Lobo, O. Mohareri, R. Rohling, and S. Salcudean are with the Department of Electrical and Computer Engineering, The University of British Columbia, Vancouver, BC V6T 1Z4, Canada.

P. Black is with the Department of Urologic Sciences, The University of British Columbia, Vancouver, BC V6T 1Z4, Canada

Color versions of one or more of the figures in this paper are available online at <http://ieeexplore.ieee.org>.

Digital Object Identifier 10.1109/TMI.2018.2810778

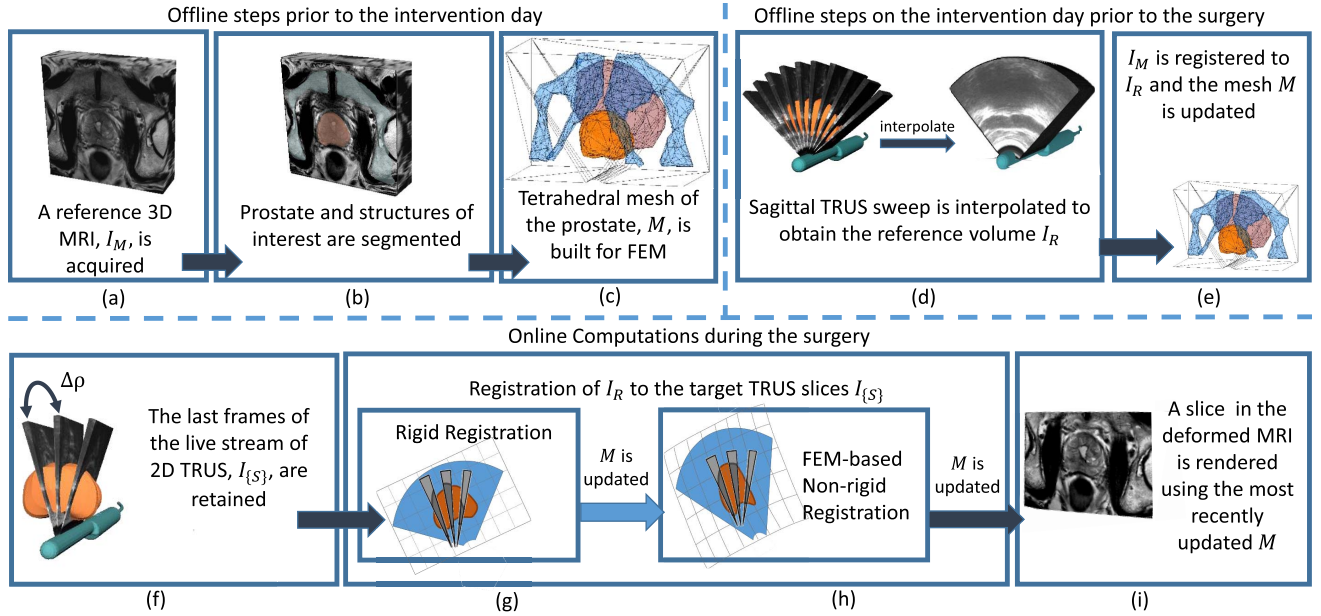


Fig. 1. Prior to the surgery (a) an MRI is acquired, (b) the prostate and the structures of interest such as the tumour are segmented by a radiologist, based on which an FEM model (c) is built. On the intervention day and as part of the surgery preparations (d) a 3D TRUS image is acquired by rotating the TRUS sagittal imaging plane fully through the prostate volume and (e) this is then deformably registered to the pre-operative MRI and the FEM mesh M is updated to match the deformation. During the surgery, (f) live 2D TRUS images are acquired. Our proposed registration is initialized based on the most recently registered mesh M and the orientation of the probe plane, and first a rigid (g) and then a deformable registration are performed. The mesh M is updated based on the deformation calculated by the registrations, and is used for the new set of 2D TRUS images.

to be registered. This provides ongoing updates to future deformations.

In this paper we focus on the latter step of 3D to 2.5D registration and present methods to carry it out fast and efficiently. An FEM model built from the pre-op 3D MRI is updated first by registering it once to an initial intra-op 3D TRUS and then repeatedly to incoming 2.5 TRUS images in real-time. This is a necessary step in our future aim of deforming the 3D MR volume and the pre-op annotations to the real-time coordinate frame of the surgery. We will be able to re-slice this volume at any desired plane position and orientation for further surgical navigation and guidance. An overview of our proposed workflow is illustrated in Fig. 1.

II. BACKGROUND

To the best of our knowledge, registration of intra-operative 2.5D TRUS to intra-operative 3D TRUS during radical prostatectomy has not been reported in the literature. Nevertheless, such methods have been proposed earlier for prostate biopsy [11]–[16]. Shen *et al.* [13] use cross-correlation to rigidly register a single ultrasound slice to a 3-D volume. They achieved a registration speed of 190 ms through computation on a Graphics Processing Unit (GPU) and down-sampling the image. However, registration of a volume to a single plane is an ill-defined problem since the out-of-plane deformations, i.e. those orthogonal to the imaged plane, cannot be estimated. Xu *et al.* [14] process multiple frames and compensate only for the rigid-body prostate motion using a sum-of-squared differences (SSD) cost function. They indicate their computation time as a limitation of their system, preventing correction of a continuous prostate motion. Krücker *et al.* [12] registered multiple 2D images simultaneously, including images with the

largest translational and rotational distance within the recent history of images. They evaluated their motion compensation only in phantom studies. Most recently, Gillies *et al.* [17] used a normalized cross-correlation (NCC) similarity metric with Powell’s method to optimize rigid registration parameters comprising of three rotations and three translations. They implemented their method on GPU and reported target registration error (TRE) and computation time of 1.6 ± 0.6 mm and 57 ± 20 ms respectively. All the methods above consider only rigid transformations of the prostate and do not take into account prostate deformations. However, while being manipulated by the surgeon, e.g. retracted and released by the grasper, the prostate may undergo considerable deformations.

Baumann *et al.* [11] compensate for the elastic deformations of the prostate, by acquiring TRUS volumes during the intervention using a 3D motorized transducer array and registering them to a reference volume through 3D-3D registration. Its relatively high computation time for 3D-3D registration (2s for rigid and 7s for elastic registration), in addition to a sweep duration of up to 5 s, makes this unsuitable for real-time AR guidance. Khallaghi *et al.* [15] consider the prostate deformations due to transducer pressure, and employ FEM for an elastic registration between a single axial 2D slice and the 3D TRUS. They aimed to analytically find the optimal deformation to avoid a slow, iterative optimization. However, for efficiency, their derivation makes the restrictive assumption by referring the pixels of a deformed volume to the FEM elements of the nominal undeformed mesh – an assumption valid only under small deformations. Moreover, their method takes 10 minutes for the registration of a single 2D slice on a CPU.

We propose an iterative registration method that can potentially handle larger deformation with higher accuracy.

Our contributions are three fold. First, we employ a computationally efficient method for slicing 2D planes in volumes deformed based on FEM. This helps to efficiently integrate an FEM-based deformation model into registration, allowing for the fast computation of gradients with respect to deformation parameters. Secondly, we propose a trust-region optimizer on analytically computed first and second derivatives of our registration cost function, which result in a speed up of orders of magnitude (88 ms per 2D slice as opposed to 10 minutes). This allows us to process multiple 2D slices at each time step (2.5D registration) and hence perform an iterative optimization, which typically converges in less than 6 iterations taking 264 ms (to process three consecutive 2D slices). Thirdly, we designed a RARLP simulator that synthesizes realistic TRUS images of the prostate that allows us to systematically analyse our registration method.

III. METHODS

The outline of our proposed system is presented in Fig. 1. The deformation model employed in our registration is a linear stress-strain quasi-static finite-element model. For this, first the prostate, bladder and the pelvic bone are segmented in a pre-operative 3D MRI volume I_M (Fig. 1b). From this segmentation, a tetrahedral mesh is created as a patient-specific deformation model of the prostate gland and its neighbouring structures (Fig. 1c). Based on FEM, the elastic response between the nodal displacements u and forces f of this discrete deformable tissue model (mesh) can be formulated as $f = Ku$, where K is called the stiffness matrix. This comprises tissue elasticity values, which could be either generic, e.g. literature reported tissue elasticities, or patient-specific, e.g. based on MRI elastography [18]. In our experiments, we used a Young's modulus and Poisson's ratio pair of (50 kPa, 0.49) for the prostate, (5 kPa, 0.45) for the bladder, and (15 kPa, 0.45) for the surrounding tissue based on [18]. The pelvic bone is considered as the fixed boundary constraint, by incorporating this in the inverse stiffness matrix K^{-1} by zeroing the elements of rows/columns corresponding to pelvic bone nodes. The above steps could all be performed prior to the surgery, immediately upon availability of an MR image and segmentation of the relevant organs.

At the beginning of the surgery, a 3D TRUS volume is collected as a set of sagittal slices by rolling the probe for a volumetric sweep. We interpolate these slices on a Cartesian grid to obtain a reference 3D TRUS volume I_R (Fig. 2). Next the pre-operative 3D MRI volume I_M is registered to this reference TRUS I_R (Fig. 1e). This could be done semi- or fully-automatically [8], [19]–[21]. In this work, we used an interactive graphical user interface to display the mesh surface overlaid on the TRUS image I_R in order to help manually reposition the prostate mesh nodes on visible prostate outline. Given these annotated prostate surface displacements as boundary constraints, the displacements of remaining nodes were calculated using the FEM. Accordingly, this brings the deformable model from MRI in the coordinate frame of the reference TRUS volume I_R .

During the surgery, a live stream of 2D TRUS sagittal images $I_{\{S\}}$ is available. On the one hand, registering the

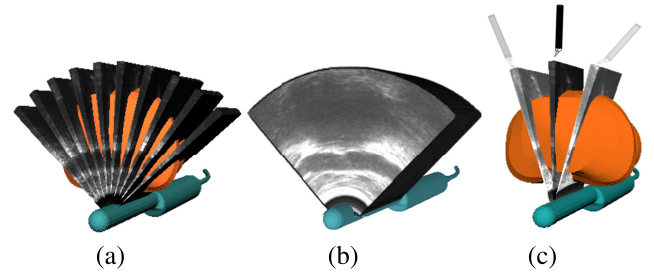


Fig. 2. (a) A 3D TRUS sweep is carried out at the beginning of the intervention to collect a set of sagittal slices (the prostate mesh is overlaid in orange). (b) These sagittal slices are interpolated to build a 3D TRUS reference volume. (c) During the surgery the probe is automatically served so that the surgical instrument tip is always on the sagittal TRUS plane. The current prostate position and deformation state are updated based on the 2.5D registration of a set of slices acquired while the TRUS transducer tracks the tool-tip.

3D reference image I_R to a single 2D real-time image I_S would suffer from out-of-plane inaccuracy, as described above. On the other hand, repeated acquisitions of full 3D volumes during the surgery might interfere with the normal course of the surgery. As a compromise, we propose to register the reference 3D TRUS I_R to a number of consecutive US images $I_{\{S\}}$ that has sufficiently large field-of-view to contain out-of-plane information, but still limited in angular range to be acquired sufficiently rapidly. We choose $I_{\{S\}}$ to cover $\approx 10^\circ$ range of roll angles (Fig. 1f). After collecting $I_{\{S\}}$, an iterative registration is performed lasting approximately 6 iterations, using the deformation field of the updated FEM model. Given subsequent sagittal images from the live stream, the above process is repeated continually during the surgery. At any instance, the FEM model deformation can be used to overlay the reference 3D MR image I_M in the current tissue deformation state.

A. Registration Framework

A summary of the notations used in the following section is presented in Table I. We employ an N -node, tetrahedral, patient-specific mesh based on segmented prostate, bladder, and pelvic bones, where the remaining value is considered to be peri-prostatic tissue (Fig. 1c). Let $\mathbf{x} = [x_{i,j}] \in \mathbb{R}^{3 \times N}$ be the matrix of 3D nodal positions, I_R be the reference TRUS volume, $I_{\{S\}}$ be a set of multiple consecutive live 2D TRUS images, and $\mathbf{p} = [p_{i,j}] \in \mathbb{R}^{3 \times M}$ be the matrix of pixel positions of $I_{\{S\}}$. The position of each pixel in I_R can be expressed in the barycentric coordinates of the enclosing tetrahedral FEM element, as a linear combination of the four tetrahedra corners. We define $\Phi = [\phi_{i,j}] \in \mathbb{R}^{N \times M}$ as a sparse interpolation function such that

$$\mathbf{p} = \mathbf{x}\Phi. \quad (1)$$

Computation of Φ for a mesh of 4-node tetrahedral elements is given in Appendix A. Let us denote the initial position of the nodes with \mathbf{x}^0 , and define the transformation

$$f(\mathbf{x}^0) = \mathbf{T}^{-1}(\mathbf{x}^0) + \mathbf{u} \quad (2)$$

consisting of a rigid transformation $\mathbf{T}^{-1}(\cdot)$ and a residual deformation (displacements) $\mathbf{u} = [u_{i,j}] \in \mathbb{R}^{3 \times N}$. Then,

TABLE I
MATHEMATICAL NOTATIONS

Symbol	Definition
N	Number of nodes in the FEM mesh
M	Number of pixels in I
$K = [K_{i,j}] \in \mathbb{R}^{3N \times 3N}$	Stiffness matrix
$x_{i,j}$	Element i of node j 's position vector
$u_{i,j}$	Element i of node j 's displacement vector
$p_{i,j}$	Element i of pixel j 's position vector
$\mathbf{x} = [x_{i,j}] \in \mathbb{R}^{3 \times N}$	Position matrix of the N nodes
$\mathbf{u} = [u_{i,j}] \in \mathbb{R}^{3 \times N}$	Deformation matrix of the N nodes
$\mathbf{p} = [p_{i,j}] \in \mathbb{R}^{3 \times M}$	Position matrix of the M pixels
$\mathbf{p}_{*i} = [p_{1,i} \ p_{2,i} \ p_{3,i}]^\top$	Position of the i^{th} pixel
\mathbf{x}^0	Initial position matrix of the mesh nodes
\mathbf{x}^t	Position matrix of the mesh nodes at time t
\mathbf{x}_{*i}^t	Position of the node i at time t
\mathbf{p}_{*i}^0	Initial position matrix of the pixels in I
\mathbf{p}_{*i}^0	Initial position of the i^{th} pixel
$\tilde{\mathbf{u}} = \mathbf{x} - \mathbf{x}^0$	Nodes' total displacement matrix
$\tilde{\mathbf{u}}_{i*}$	i^{th} row of $\tilde{\mathbf{u}}$
$I_{\{S\}}$	A set of 2D TRUS
I_R	The reference TRUS volume
I_M	The reference MRI volume
$G_{i,i} = 1, 2, 3$	Gradient of I_R in the i^{th} dimension
$\Phi = [\phi_{i,j}] \in \mathbb{R}^{M \times N}$	FEM interpolation matrix
Φ_{*i}	i^{th} column of Φ
K_{*i}	i^{th} column of K
$\omega = [\omega_i] \in \mathbb{R}^6$	Rigid Transform Parameters
$\mathbf{J} = [J_{j,i}] \in \mathbb{R}^{3 \times 6}$	Jacobian matrix of \mathbf{T} in Eq.3

the registration task is equivalent to finding the transformation $f(\cdot)$ under which the deformed volume I_R is best aligned with the set of 2D slices $I_{\{S\}}$. One approach of finding the optimal $f(\cdot)$ would be to deform the volume I_R based on a candidate $f(\cdot)$ and then re-slice it at the imaged planes in $I_{\{S\}}$ to compare their intensity values with $I_{\{S\}}$. However, this is computationally intensive and also unnecessary, since in the undeformed volume I_R only the intensity values at the relatively fewer locations \mathbf{p}^0 , i.e. those corresponding to \mathbf{p} in $I_{\{S\}}$, are required for any comparison. In the next sections, we will elaborate on how we calculate \mathbf{p}^0 for the rigid and deformable registration steps. Fig. 3 demonstrates our framework in the axial plane, in 2D for illustration purposes. Therein a reference TRUS volume (shown as a 2D axial slice in Fig 3a) is seen to be first rigidly (Fig 3b) and next non-rigidly (Fig 3c) registered to multiple 2D slices (shown as wedges in Fig 3c).

B. Rigid Registration

Let $R_\theta, \theta \in \mathbb{R}^3$ be a rotation function (defined in Appendix A), $\tau \in \mathbb{R}^3$ a translation and $\omega = [\theta^\top, \tau^\top]^\top = [\omega_i] \in \mathbb{R}^6$. We define

$$\mathbf{T}(\mathbf{p}, \omega) = R_\theta(\mathbf{p}) + \tau \quad (3)$$

as a homogenous transformation with rotation R_θ and translation τ .

Ignoring the deformation term \mathbf{u} in Eq.(2),

$$\mathbf{p}^0 = \mathbf{T}(\mathbf{p}, \omega) \quad (4)$$

and the optimum ω can be defined to minimize, e.g., the SSD

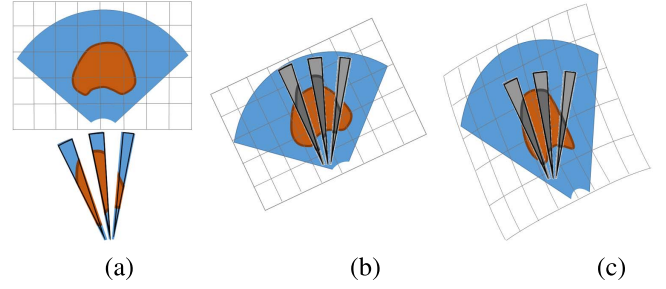


Fig. 3. The visualization of our registration steps in 2D. (a) The inputs to the registration algorithm. On top a transverse view of the reference 3D TRUS volume (I_R) with the corresponding FEM mesh and on bottom three target 2D sagittal slices ($I_{\{S\}}$). (b) Rigidly and (c) non-rigidly registered reference volume overlaid with $I_{\{S\}}$.

cost function, i.e.

$$C_r(\mathbf{p}, \omega) = \frac{1}{2} \|D(\mathbf{p}, \omega)\|_2^2. \quad (5)$$

with $D(\mathbf{p}, \omega) = I_R(\mathbf{p}^0) - I_{\{S\}} = I_R(\mathbf{T}(\mathbf{p}, \omega)) - I_{\{S\}}$ being the difference over the support of I_S .

The optimal transformation parameters ω are found herein by minimizing the SSD cost function $C_r(\mathbf{p}, \omega)$ based on a trust-region optimizer using its first derivative

$$\begin{aligned} \frac{\partial C_r(\mathbf{p}, \omega)}{\partial \theta_k} &= D(\mathbf{p}, \omega)^\top \frac{\partial D(\mathbf{p}, \omega)}{\partial \omega_k} \\ &= \sum_{i=1}^N D(\mathbf{p}_{*i}, \omega) \sum_{j=1}^3 \frac{\partial I_R(\mathbf{T}(\mathbf{p}_{*i}, \omega))}{\partial T_j(\mathbf{p}_{*i}, \omega)} \frac{\partial T_j(\mathbf{p}_{*i}, \omega)}{\partial \omega_k} \\ &= \sum_{i=1}^N D(\mathbf{p}_{*i}, \omega) \sum_{j=1}^3 G_j(\mathbf{T}(\mathbf{p}_{*i}, \omega)) J_{j,k}(\mathbf{p}_{*i}, \omega) \end{aligned} \quad (6)$$

and second derivative. By ignoring higher than quadratic terms we have:

$$\frac{\partial^2 C_r}{\partial \omega_k \partial \omega_m} \approx \frac{\partial D}{\partial \omega_k} \frac{\partial D}{\partial \omega_m} \quad (7)$$

$$= \sum_{i=1:3} \sum_{j=1:3} G_i J_{i,k} G_j J_{j,m} \quad (8)$$

where \mathbf{p}_i is the 3D position of the i^{th} pixel, G_j is the gradient of I_R in the j^{th} direction, and $\mathbf{J} = [J_{j,i}] \in \mathbb{R}^{3 \times 6}$, $J_{j,i} = \frac{\partial T_j}{\partial \omega_i}$ is the Jacobian matrix of the transformation \mathbf{T} .

C. Deformable Registration

To define a cost function for the deformable registration, we extend the rigid transformation assumption in Eq. 5 with the previously-neglected deformable term \mathbf{u} , in order to regularize displacements by penalizing biomechanically implausible configurations of FEM nodes, introduced by the strain energy ($\text{vec}(\mathbf{u})^\top K \text{vec}(\mathbf{u})$) as follows:

$$C_d(\mathbf{u}, \mathbf{p}) = \frac{1}{2} \|D(\mathbf{u}, \mathbf{p})\|_2^2 + \frac{\alpha}{2} \text{vec}(\mathbf{u})^\top K \text{vec}(\mathbf{u}), \quad (9)$$

where $D(\mathbf{u}, \mathbf{p}) = I_R(\mathbf{p}^0) - I_{\{S\}}$ and α is a regularization constant.

In order to simplify the derivations for deformable registration, we introduce $\tilde{\mathbf{u}} = \mathbf{x} - \mathbf{x}^0$, which is the total displacement of nodes including their rigid transformation and deformation, i.e.

$$\mathbf{p}^0 = \mathbf{x}^0 \Phi = \mathbf{p} - \tilde{\mathbf{u}} \Phi. \quad (10)$$

The first derivative of C_d can then be computed similarly to Eq. 6, yielding

$$\begin{aligned} \forall m \in \{1, 2, 3\}, \quad \forall n \in \{1, \dots, N\} \\ \frac{\partial C_d}{\partial u_{m,n}} = - \sum_{i=1}^N \sum_{j=1}^3 (I_R(\mathbf{p}_{*i}^0) - I_{\{S\}}) G_j(\mathbf{p}_{*i}^0) \frac{\partial p_{i,j}^0}{\partial u_{m,n}} \\ + \alpha \text{vec}(\mathbf{u})^\top K_{3(n-1)+m} \quad (11) \end{aligned}$$

with $K_{\cdot i}$ denoting the i^{th} column of K , and $K_{i,j}$ being the element on the i^{th} row and j^{th} column of K . The partial derivative of corresponding nominal pixel locations \mathbf{p}^0 with respect to each nodal displacement component $u_{m,n}$ can be written as

$$\frac{\partial p_{i,j}^0}{\partial u_{m,n}} = \frac{\partial (p_{i,j} - \tilde{\mathbf{u}}_{*i}^\top \Phi_{*j})}{\partial u_{m,n}} = - \sum_{l=1}^N \frac{\partial (u_{i,l} \phi_{l,j})}{\partial u_{m,n}} \quad (12)$$

where Φ_{*i} is the i^{th} column of Φ and $\tilde{\mathbf{u}}_{*j}$ is the j^{th} row of $\tilde{\mathbf{u}}$. Assuming the relative positions of nodes within each element will change minimally between incremental steps of a deformation, we can linearize around the given deformation state by ignoring any changes in the FEM basis functions due to nodal changes, such that

$$\forall j, l, m, n \quad \frac{\partial \phi_{l,j}}{\partial u_{m,n}} = 0 \quad (13)$$

Thus, the first derivative in Eq.11 can be rewritten as

$$\begin{aligned} \frac{\partial C_d}{\partial u_{m,n}} = - \sum_{i=1}^N (I_R(\mathbf{p}_{*i}^0) - I_{\{S\}}) G_m(\mathbf{p}_{*i}^0) \phi_{i,n} \\ + \alpha \text{vec}(\mathbf{u})^\top K_{3(n-1)+m}, \quad (14) \end{aligned}$$

and the second derivative of C_d follows similarly from the above and Eq. 8 as follows:

$$\begin{aligned} \frac{\partial^2 C_d}{\partial u_{m,n} \partial u_{l,k}} = \sum_{i=1}^N \sum_{j=1}^N G_m(\mathbf{p}_{*i}^0) \phi_{i,n} G_l(\mathbf{p}_{*i}^0) \phi_{j,k} \\ + \alpha K_{3(n-1)+m, 3(k-1)+j}. \quad (15) \end{aligned}$$

To evaluate the cost function as well as its derivatives, at every optimization iteration we need to calculate Φ , $I_R(\mathbf{p}^0)$, $G_1(\mathbf{p}^0)$, $G_2(\mathbf{p}^0)$, and $G_3(\mathbf{p}^0)$ for all the imaged planes in I . We propose to speed up these computation in two ways. Firstly, we note that the gradients of the preoperative image volume I_R in all three dimensions, G_1, G_2, G_3 are independent of the transformations (rigid and deformable). Therefore, we compute these once at the beginning of the registration to be employed thereafter in all registration iterations. However, the sampling points $\mathbf{p}^0 = \mathbf{p} - \tilde{\mathbf{u}} \Phi$ in Eq.10 need to be computed at every iteration, since they depend on the locations \mathbf{p} of the imaged slices I , as well as the deformation \mathbf{u}^* , which evolves with the registration parameters. This necessitates the

calculation of Φ at each iteration, which involves finding the enclosing finite element for all pixels \mathbf{p} in I . This is generally computationally very intensive and poses a great challenge to fast convergence of the optimization of FEM-based registrations. As our second measure to speed up the registrations, we use a fast method to compute Φ and propose to simultaneously re-slice all four volumes (I_R , G_1 , G_2 , and G_3 – all under a deformation $\tilde{\mathbf{u}}$) at pixels \mathbf{p} of the given imaging planes I in real time (on average in 5ms for a resolution of 144×124 for an FEM mesh with 1552 nodes). This algorithm for fast synthesis of 2D slices in a deformed 3D volume, which presented in [22], consists of the following steps :

For each pixel \mathbf{p}_i , $i \in \{1..M\}$

- (I) Find the finite element e_s enclosing \mathbf{p}_i
- (II) Find its undeformed position \mathbf{p}_{*i}^0 based on the nodal displacements of e_s and the basis function Φ
- (III) Interpolate the given data (I_R, G_1, G_2 and G_3) at \mathbf{p}_{*i}^0

Steps (II) and (III) above are constant-time operations, for which there exist well-studied fast implementations. However, the point location problem of step I is computationally demanding and hence the bottleneck of this technique.

For the synthesis of a frame, first the set of elements $\{e_s\}$ that are intersected by the 2D TRUS imaging plane is compiled. This set is composed by traversing the elements in the plane using a 3-D mesh element neighborhood list, which is precompiled offline as soon as a 3D mesh is available. This is possible as the neighbors of an element do not change with deformation. Given an intersected element, such a list enables us to deduce its neighbors that are also intersected by observing which face of the current element intersects the image plane. The set $\{e_s\}$ is then sorted topologically and an arbitrarily chosen direction (e.g., top-faces) of the element projections are discretized [22] at the image pixels, e.g. via Bresenham's line drawing algorithm [23], to be marked on the image in that sorted order. The above mesh-image intersection is the only information needed to locate all image pixel points. Indeed, assuming a traversal of image pixels in the chosen direction above (i.e., top-to-bottom), if no face (discretized line) is crossed when moving from a pixel to its neighbor, the latter pixel can then be concluded to lie in the very same element. Accordingly, once this discretized face structure is constructed, a simple traversal allows us to assign each pixel to a mesh element in constant time (at the computational cost of checking a pixel value).

The element map building step (I) can be summarized as:

- (A) Compile the set $\{e_s\}$ of intersected elements, with their partial ordering relations with respect to a chosen traversal direction, e.g. top-bottom
- (B) Sort $\{e_s\}$ topologically
- (C) Mark the (top) cross sections of $\{e_s\}$ on the image pixels in the sorted order, by labeling these with corresponding intersecting element (s)
- (D) Traverse the image with parallel scan lines
 - (a) if the pixel p_i is marked, set the label as the *current* element s
 - (b) Assign pixel \mathbf{p}_i to element e_s
 - (c) Traverse to next point (\mathbf{p}_{i+1}) and go to (a)

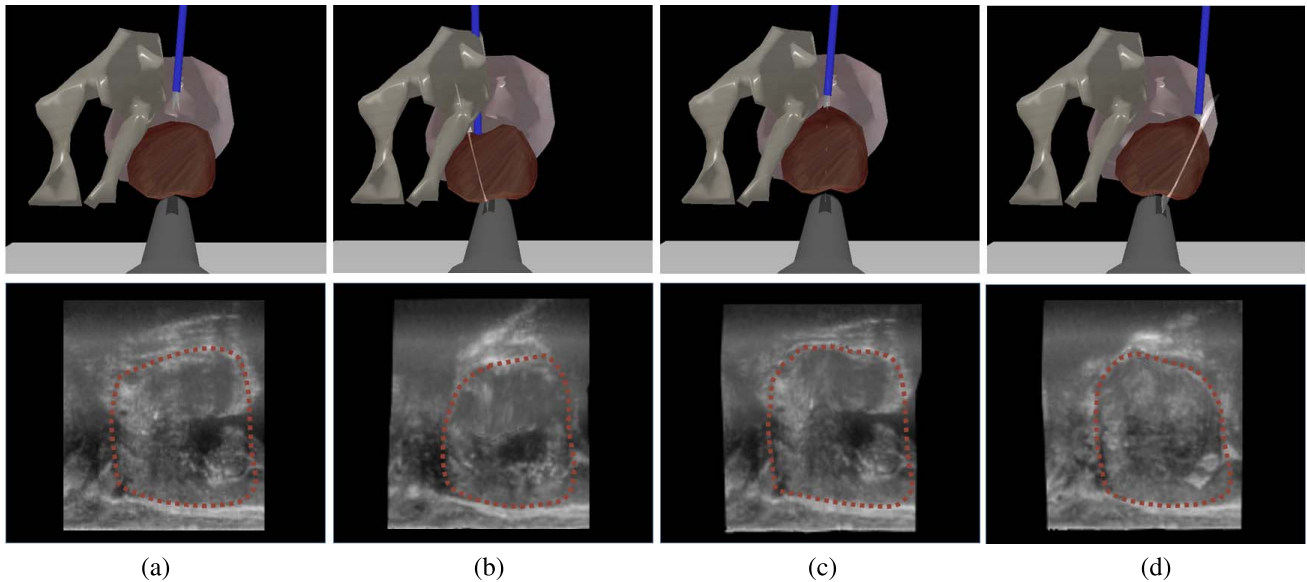


Fig. 4. Snapshots of our simulator during data synthesis. Top row (a) displays the resting state, (b) pressing, (c) retracting of the prostate upwards and (d) laterally. The corresponding simulated sagittal ultrasound images are presented on the bottom row. Note that the left portion of the pelvic bone has been made invisible to allow better visualization of the deformations.

Note that the above is a special case of point-in-element problem, where the requested points (of images I in our case) lie on a dense (Cartesian) grid, yielding itself to the presented fast treatment. It can be shown that when $M \gg N$, the running time of the above algorithm is $O(M)$ which is also the lower bound since to render an image each pixel has to be processed at least once (see [22] for a detailed analysis). Conversely, the brute-force method where for each pixel is checked whether it is inside an element would have a running time of $O(NM)$. Any other alternative method would still require at least one in-element check, that would require to compute the barycentric coordinates of each given point, even for all correct prior guesses, in addition to other (heuristic) operations if this check fails.

IV. EXPERIMENTS AND RESULTS

We evaluated our proposed method by conducting a set of experiments using simulated and patient data. For all our experiments, we used a fixed value of $\alpha = 0.1$ in Eq. 9.

A. Materials

In our experiments, we used data from 7 patients undergoing prostatectomy (P1-P7) and 4 patients undergoing focal therapy (F1-F4), all of whom had informed consent in institutional review board approved studies. All of the 3D images in our datasets were reconstructed TRUS sweeps obtained by rotating an ultrasound transducer by a motorized brachytherapy cradle (see Fig. 2). We used a BK Pro-Focus ultrasound system (BK Medical, Herlev, Denmark) with a biplane TRUS (transverse micro-convex/axial) 8848 4-12 MHz probe. The TRUS probe was rolled around its axis in 0.9° increments (90° in total) to collect 100 sagittal images of 138×120 pixel resolution, with a depth of 60 mm and a width of 69 mm. Note that to record ultrasound images that were

synchronized with the motor roll angle, we had to save the raw radiofrequency data (RF) through a frame-grabber, and the processing algorithms we then had to use to generate B-mode images from such RF data are unfortunately not comparable to commercial solutions. Moreover, we acquired sagittal slices during a TRUS roll, which were later interpolated on a 3D grid for the volumes, which thus leads to lower elevational resolution. These factors account for the sub-par quality of the images in our dataset compared to clinical TRUS images.

B. Radical Prostatectomy Simulations

To quantitatively study the performance of our proposed method, we developed a simulator that can generate realistic TRUS images during TRUS-guided RARLP procedure. In our approach, designed for the Da Vinci[®] surgical system (Intuitive Surgical Inc., Sunnyvale, CA, US) a motorized TRUS cradle holding the probe is automatically controlled such that the Da Vinci instrument tip always lies in the TRUS imaging plane [24] (see Fig. 2c). In our procedure, we can move the Da Vinci tool tip, grasp and apply forces to the prostate tissue, which then deforms based on a patient-specific FEM of the prostate and surrounding tissue. Given this as ground-truth deformation, we then validate our registration algorithm for the simulated TRUS images in the deformed tissue state. This simulator is based on an earlier training system developed for prostate brachytherapy, described in [25]. We used the image data of patient P1 in our simulations. Fig. 4 displays snapshots of our simulator with the images on the top row generated at the initial state and the image of the lower rows generated during compression and retraction of the organ. The corresponding simulated sagittal ultrasound images are presented in the bottom row of Fig. 4.

In order to model tissue deformations in this simulator, the tetrahedral mesh from the segmented MRI volume of

TABLE II

STATISTICS (MEAN \pm STD (MAX)) OF THE REGISTRATION ERROR IN mm OVER 4 SEQUENCES INCLUDING A TOTAL OF 912 TIME STEPS DESCRIBED BY MEAN OF THE EUCLIDEAN DISTANCE OF THE SYNTHETICALLY DEFORMED *Involved Nodes* AND THEIR RECOVERED POSITION AFTER REGISTRATION

$2\Delta\rho$	Initial Deformation	Rigid Registration	Deformable Registration
3°	3.89 ± 2.23 (10.39)	1.63 ± 0.77 (4.95)	1.60 ± 0.86 (4.87)
5°	3.89 ± 2.23 (10.39)	1.60 ± 0.73 (4.84)	1.22 ± 0.53 (4.46)
10°	3.89 ± 2.23 (10.39)	1.56 ± 0.68 (4.57)	1.15 ± 0.47 (3.66)

patient P1 is used. Using FEM, for given interaction forces a quasi-static solution for the deformation state can be found as $u = K^{-1}f$. The roll angle ρ of the probe is computed automatically based on the current instrument tip position, i.e. to keep it in the TRUS plane [24] (see Fig. 2c). To evaluate sensitivity to angular span $\Delta\rho$, for every evaluation configuration (tool/grasp configuration) we simulated the acquisition of three sets of US images : Each set containing two with roll angles $\rho \pm \Delta\rho$, $\Delta\rho \in \{1.5^\circ, 2.5^\circ, 5^\circ\}$, in addition to one with the center roll angle ρ . We define *relevant nodes* as the set of all the nodes in the elements intersecting the slice with roll angle ρ . We used the same FEM mesh as the simulator in our registrations. For validation we compared the position of the relevant nodes at time step $t \in \{1 \dots T\}$ recovered from registration, $\hat{\mathbf{x}}_{*n}^t$, $n \in \{\text{relevant nodes}\}$, with their actual position output by the simulator \mathbf{x}_{*n}^t . The reported errors, E , are the mean of the Euclidean norm of the differences of these two values:

$$E = \frac{1}{T \cdot N_r} \sum_t \sum_{n \in \{\text{relevant nodes}\}} \|\mathbf{x}_{*n}^t - \hat{\mathbf{x}}_{*n}^t\|,$$

with N_r being the number of relevant nodes. This provides a lower bound as the position of the voxels enclosed by the relevant nodes are a positively weighted sum of the relevant nodes and hence their registration error should be smaller or equal to them. This error evaluation method obviates the need for manual landmark selection which might suffer from inter-subject variability and out-of-plane errors. We repeated our registration experiment with the 3 different values of $\Delta\rho$, each time taking into account the 3 frames $\{\rho - \Delta\rho, \rho, \rho + \Delta\rho\}$. We assessed our method on 4 sequences each containing between 200 to 250 time steps resulting on a total of 912 time steps. These validation sequences consisted of the prostate being grasped and retracted laterally and superiorly (see Fig. 4). The average and maximum displacements of the prostate nodes were 3.89 mm and 10.39 mm respectively. Our method achieved a mean error of 1.15 mm, which is over 25% improvement over the rigid registration error of 1.56 mm as seen in Table II.

A larger span of 10° as seen in Table II produced the lowest errors. Fig. 5 displays an example with the original simulated 2D slice and the registered image after the rigid and the deformable steps. Fig. 6 demonstrates the average deformation of the prostate mesh nodes as well as the average rigid and deformable registration error over all the relevant nodes during one of the simulation sequences.

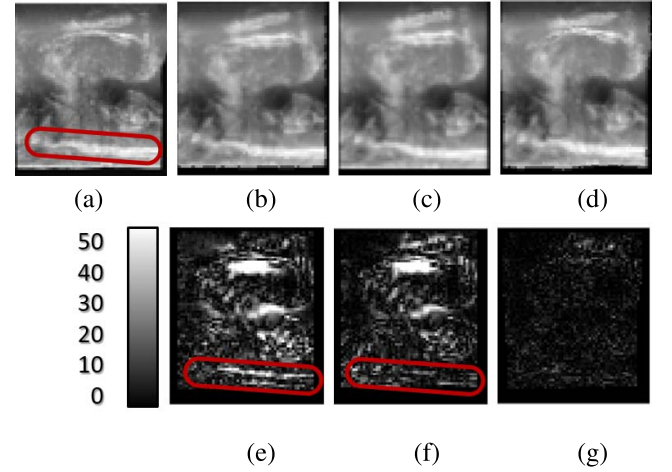


Fig. 5. (a) A synthetic 2D sagittal TRUS image with 4.10 mm of average deformation per FEM node. The synthesized images (b) prior to registration (c) after rigid registration with 3.55 mm average error (d) and after deformable registration with 1.62 mm average error. (e-g) display the difference between the synthesized and the resampled images within the segmentation mask. It could be observed in (e) and (f) that the rectal wall (annotated with red) has been aligned after the rigid registration, but the prostate deformations are only compensated after the deformable registration (g).

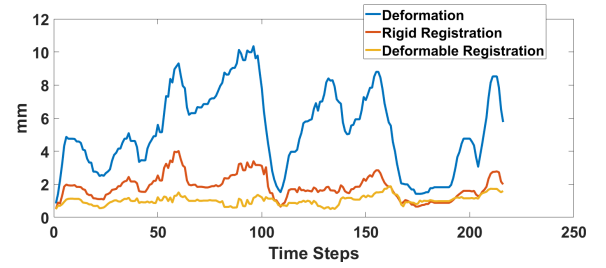


Fig. 6. The registration results on a sequence of 215 time steps, with 3 adjacent slices covering a span of $2\Delta\rho = 10^\circ$ degrees. The mean values for the deformation, rigid and deformable registration errors are computed for the relevant nodes.

It should be noted that during the simulation the magnitude and direction of the forces on every mesh node is known and rendering the images is a straight-forward task. However, during the registration, neither the forces nor the displacements of the mesh nodes are known. At each iteration, an estimate of the node displacements is updated such that the intensity-based registration cost function Eq. 9 is minimized. The regularization term may affect the location of the global minimum, and based on image content (smoothness) registration might be caught at a local minimum – different than the simulated ground-truth nodal deformation. Therefore, our method did not produce zero errors, in spite of using the same FEM mesh (forward model) as the simulator.

The method takes on average 13 ms and 75 ms per 2D slice, for the rigid and deformable registration respectively, on an i7-6700 central processing unit (CPU) at 3.4GHz (Intel Corporation, Santa Clara, CA, USA). Hence for a three-slice registration the total registration time is 264 ms.

C. Patient Data

In our datasets, we had a series of 3D TRUS sweeps acquired prior to intervention and a series of 3D TRUS sweeps

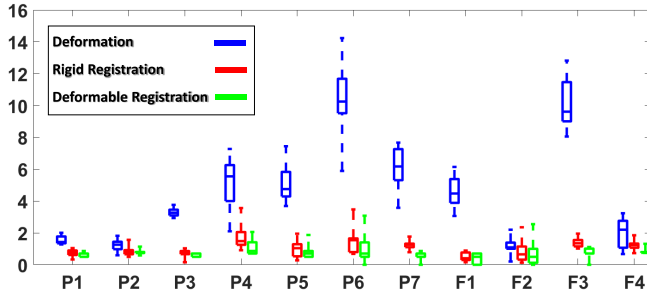


Fig. 7. The distribution of the initial error of the selected landmarks for each patient as well as those of their rigid and deformable registration errors are illustrated with a box plot. It can be seen that the accuracy is consistently improved from rigid registration to the deformable registration.

TABLE III

STATISTICS (MEAN \pm STD (MAX) IN mm) OF THE REGISTRATION ERROR IN mm DESCRIBED BY THE AVERAGE EUCLIDEAN DISTANCE OF A SET OF LANDMARKS ON THE TARGET VOLUME WITH THEIR CORRESPONDING LANDMARKS ON THE INITIAL, RIGIDLY AND NON-RIGIDLY REGISTERED REFERENCE VOLUME

	Initial Deformation	Rigid Registration	Deformable Registration
P1	1.54 \pm 0.26 (2.01)	0.74 \pm 0.22 (1.05)	0.60 \pm 0.14 (0.87)
P2	1.23 \pm 0.32 (1.82)	0.84 \pm 0.28 (1.57)	0.73 \pm 0.15 (1.12)
P3	3.29 \pm 0.24 (3.76)	0.74 \pm 0.20 (1.03)	0.61 \pm 0.11 (0.71)
P4	5.16 \pm 1.56 (7.27)	1.72 \pm 0.72 (3.56)	1.11 \pm 0.45 (2.06)
P5	5.15 \pm 1.17 (7.44)	1.00 \pm 0.47 (1.95)	0.80 \pm 0.42 (1.87)
P6	10.55 \pm 2.17 (14.23)	1.43 \pm 0.71 (3.48)	0.97 \pm 0.79 (3.08)
P7	6.14 \pm 1.24 (7.67)	1.22 \pm 0.26 (1.77)	0.56 \pm 0.20 (0.87)
F1	4.56 \pm 0.89 (6.14)	0.50 \pm 0.25 (0.89)	0.34 \pm 0.33 (0.71)
F2	1.19 \pm 0.46 (2.20)	0.83 \pm 0.65 (2.35)	0.74 \pm 0.77 (2.55)
F3	10.12 \pm 1.59 (12.82)	1.38 \pm 0.27 (1.96)	0.74 \pm 0.30 (1.12)
F4	1.93 \pm 0.90 (3.24)	1.21 \pm 0.26 (1.85)	0.76 \pm 0.14 (1.22)
total	4.62 \pm 3.38 (14.23)	1.05 \pm 0.55 (3.56)	0.72 \pm 0.45 (3.08)

acquired during the intervention. One pre-operative 3D TRUS sweep was interpolated to create a *preop* volume with the isotropic voxel size of $0.5 \times 0.5 \times 0.5 \text{ mm}^3$. This volume was used as our reference image I_R (see Fig. 1d). For each test, we extracted 3 sagittal slices from an intra-operative 3D TRUS sweep with an angle of $\Delta\rho = 5.4^\circ$ between each pair (which is the closest to $\Delta\rho = 5^\circ$, given the angular step size of 0.9° , see Fig. 1f). We then registered the reference preop volume to these target slices (see Fig. 2).

For each registration we selected 5 sets of landmark points on each target slice, resulting in a total of 15 points $\{p_0\}$. The corresponding points were selected on the reference image I_R and are referred to as $\{p_1\}$. These landmarks included calcifications or vascular structures on and around the prostate gland that were identifiable in both the reference, I_R , and the target images, $I_{[S]}$. For each patient, we report the average error over these 15 points. The rigid and deformable transformations resulting from the registration were applied to the points $\{p_1\}$, resulting in p_R and p_D . Accordingly, for each landmark the initial error ($E_I = \|p_0 - p_1\|$), the rigid registration error ($E_R = \|p_0 - p_R\|$), and the deformable registration error ($E_D = \|p_0 - p_D\|$) were calculated.

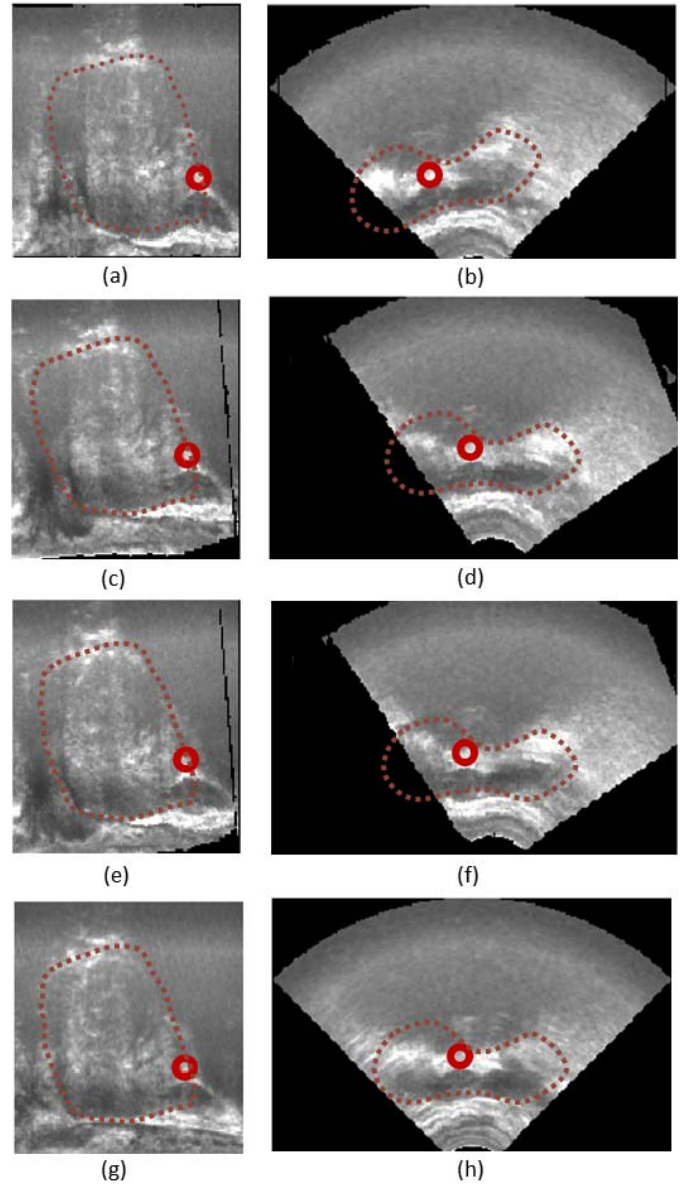


Fig. 8. (a,b) Sagittal and axial slices in the reference volume V_I , (c,d) in the rigidly registered volume V_R and (e,f) in the non-rigidly reference volume V_D . images (g) and (h) are the corresponding sagittal and axial slices in the target TRUS volume. The red circle denotes a selected landmark in this target volume and its counterparts in all other volumes. The prostate is delineated by the red contours.

The quantitative results on all the datasets are presented in Table III and Fig. 7. It can be seen that the rigid registration has an error of 1.05 mm on average, and that the deformable registration improved this to 0.72 mm. The deformable registration has also reduced the maximum error from 3.56 mm to 3.08 mm. The largest reduction of error occurs for cases with the largest initial deformations (P4, P6, P7 and F3). We performed paired t-test on rigid and deformable registration results for each patient to see if the latter was significantly different from the former. This was the case for 8 out of 11 patients. The three patients with no significant reduction (P2, P3 and F2) had sub-millimeter rigid registration errors. Fig. 8 displays an example of a 2D slice

from the target volume (P7), and the corresponding slices in the registered reference images.

V. DISCUSSION AND CONCLUSION

Previously proposed methods either provide fast computation with single-slice rigid registration [17], or deformable registrations that cannot be computed in real-time [10], [15]. To the best of our knowledge, our work is the first reported deformable registration with multiple frames that can be carried out in real-time (264 ms). The core re-slicing operation of the volumes was implemented in C++ and imported as a mex function into Matlab. The rest of the code including the optimization is in Matlab, run on CPU. We expect to further improve the speed of our method by exporting the entire code to C++ and running it on GPU.

The literature on 3D-2D TRUS registration of prostate images is mainly concerned with biopsy procedures, in which the nature of prostate manipulation is different from surgical procedures such as prostatectomy. In biopsy, even though the transducer pressure might cause deformations to the interior of the prostate, a rigid registration might be sufficient. However, rigid registration will not be sufficient in the presence of substantial tissue deformations, especially during RARLP. As our simulations have shown, even in the presence of an average of 3.89 mm displacement of the outer prostate nodes, a considerable deformation is introduced internally, which cannot be recovered merely by rigid registration.

The use of our fast slicing method to compute image intensity for slices under deformation in registration is our main novelty. However, this technique significantly impacts the optimizer. Indeed, at every iteration both the cost functions and the gradients are needed, both of which require this *fast slicing*. Used in a naive way with a numerical optimizer, the convergence would be slower, preventing real-time performance. This is prevented by our analytical computation of the derivatives of the cost function. Moreover, we further accelerate the optimization for the gradient computation by *pre-computing gradients only once (offline) on our reference image, which then obviates the need to generate a full deformed volume for computing the gradients on a slice. These novel uses of the fast image intensity computation allow our method to converge very quickly after (on average) only 4 fast slicing function calls.*

During prostatectomy our proposed guidance system can run for as long as the TRUS images of the prostate are available, i.e. the prostate touches the probe. Hence, the guidance will be running and useful while the surgeon is still cutting nerves, veins, lymph nodes and fatty tissues connected to the organ. When the prostate is lifted from the rectum, the air entering this gap undermines the propagation of the ultrasound waves through the organ tissue. Nevertheless, this happens only in few cases as reported in Mohareri *et al.* [4]: Out of 20 surgeries, the Montsouris approach (initial posterior dissection of the prostate and seminal vesicles) was used only in few cases, which were those with subsequent TRUS image quality been affected negatively due to insufflation gas entering posterior to the prostate.

Since neurovascular bundles (NVBs) are of concern to the surgeon, the errors at these regions are important. However, NVBs are not recognizable in ultrasound B-mode images, and often not recognizable in MRI T₂ images. Therefore, we had no reliable way of directly quantifying the error in NVB location. The landmarks used in the error computation have been selected on and around the prostate so that they are very likely to also include the NVBs. In future work, we plan to add NVB annotation in MRI images, whenever possible, and also explore if the addition of power Doppler to the B-mode images may not help with NBV localization.

Our patient data show that although the rigid registration compensates for any bulk motion, there remain residual errors that are significantly reduced in most cases after deformable registration. Furthermore, our deformable registration can be executed in real-time and presents a general solution to updating the prostate configuration and hence the cancer location during image-guided RARLP.

We also introduced a method of registration evaluation using simulated TRUS images, which allows for reliable ground truth as well as a systematic evaluation of the method performance under different deformations. Future work is planned for integrating our method in a robotic surgical suite for an in-vivo assessment.

APPENDIX A COMPUTING THE FEM INTERPOLATION MATRIX IN A TETRAHEDRAL MESH

The 3D position of a point $\mathbf{p}_i = [p_{i,1} \ p_{i,2} \ p_{i,3}]^T$ inside a tetrahedral element e with $k=4$ element nodes as $\mathbf{x}_k^e = [x_{k,1}^e \ x_{k,2}^e \ x_{k,3}^e]^T$ can be expressed in normalized coordinates in terms of barycentric coordinates r_k as

$$\mathbf{p}_i = \sum_{k=1}^4 r_{i,k} \mathbf{x}_k^e \quad (16)$$

$$\begin{bmatrix} p_{i,1} \\ p_{i,2} \\ p_{i,3} \\ 1 \end{bmatrix} = \begin{bmatrix} x_{1,1}^e & x_{2,1}^e & x_{3,1}^e & x_{4,1}^e \\ x_{1,2}^e & x_{2,2}^e & x_{3,2}^e & x_{4,2}^e \\ x_{1,3}^e & x_{2,3}^e & x_{3,3}^e & x_{4,3}^e \\ 1 & 1 & 1 & 1 \end{bmatrix} \begin{bmatrix} r_{i,1} \\ r_{i,2} \\ r_{i,3} \\ r_{i,4} \end{bmatrix} \quad (17)$$

$$\mathbf{p}_i = \mathbf{X}^e \mathbf{r}_i \quad (18)$$

Thus, the barycentric coordinates $\mathbf{r}_i = (\mathbf{X}^e)^{-1} \mathbf{p}_i$.

To build Φ , for each row $i \in \{1..M\}$, we set the columns corresponding to the nodes enclosing \mathbf{p}_i to their barycentric coordinates and the rest to zero, i.e.

$$\phi_{i,j} = \begin{cases} r_{i,k}, & \text{if } \mathbf{x}_j \text{ is node } k \text{ of } e_i, \\ 0, & \text{otherwise} \end{cases}, \quad \begin{matrix} \forall i \in \{1..M\} \\ \forall j \in \{1..N\} \end{matrix} \quad (19)$$

for e_i denote the nodes enclosing \mathbf{p}_i .

APPENDIX B CALCULATION OF THE JACOBIAN FOR THE RIGID TRANSFORMATION

Herein we calculate the Jacobian \mathbf{J} of the transformation \mathbf{T} with respect to the rotation parameters $\boldsymbol{\theta}$ such that $\mathbf{J}_{i,j} = (\frac{\partial T_i}{\partial \theta_j})$, assuming that the transformation is separated into rotational and translational components. Note that parameterizing $\boldsymbol{\theta}$ in

Euler angles has the problem of not lying in an Euclidean space. Thus, we resort to Lie groups where the set of all rotations constitute an $SO(3)$ group and hence can be embedded on a manifold in \mathbb{R}^9 space. The parameters of the rotations could be approximated linearly around a specific point on the manifold and the mapping between the parameters on the manifold and the Euclidean coordinate system can be performed using exponents. Thus, we define $\theta = [\theta_1\theta_2\theta_3]$.

Current rotation R_θ can be obtained by the rotation of an initial frame R_0 by an incremental rotation $R\theta^+$, i.e.

$$R_\theta = R_0 R_\theta^+, \quad \text{where} \quad (20)$$

$$R_\theta^+ = \exp(S(\theta)) = \exp \begin{pmatrix} 0 & -\theta_3 & \theta_2 \\ \theta_3 & 0 & -\theta_1 \\ -\theta_2 & \theta_1 & 0 \end{pmatrix} \quad (21)$$

which then leads to the partial derivatives

$$\mathbf{J}^{3 \times 6} = \frac{\partial \mathbf{T}}{\partial \theta_i} = R_0 \frac{\partial (R_\theta^+ \mathbf{p} + \mathbf{d})}{\partial \theta_i} = [\nabla R_\theta \mathbf{I}^3] \quad (22)$$

$$\nabla R_\theta = R_0 \frac{\partial (\exp(S(\theta)))}{\partial \theta_i} \mathbf{p} \quad (23)$$

$$= R_0 \exp(S(\theta)) \frac{\partial (S(\theta))}{\partial \theta_i} \mathbf{p} \quad (24)$$

$$= R_0 \exp(S(\theta)) L_i \mathbf{p} \quad (25)$$

where $L_i = \frac{\partial (S(\theta))}{\partial \theta_i}$, i.e.

$$L_1 = \begin{pmatrix} 0 & 0 & 0 \\ 0 & 0 & -1 \\ 0 & 1 & 0 \end{pmatrix}, \quad L_2 = \begin{pmatrix} 0 & 0 & 1 \\ 0 & 0 & 0 \\ -1 & 0 & 0 \end{pmatrix},$$

$$\text{and } L_3 = \begin{pmatrix} 0 & -1 & 0 \\ 1 & 0 & 0 \\ 0 & 0 & 0 \end{pmatrix}. \quad (26)$$

Accordingly,

$$\nabla R_\theta = R_0 \exp(S(\theta)) (L_1 \mathbf{p} \quad L_2 \mathbf{p} \quad L_3 \mathbf{p}) \quad (27)$$

$$= R_0 \exp(S(\theta)) S(-\mathbf{p}) \quad (28)$$

ACKNOWLEDGEMENTS

The authors would like to thank the early postdoc mobility fellowship from the Swiss National Science Foundation (SNSF).

REFERENCES

- [1] D. W. Cool *et al.*, "Repeat prostate biopsy accuracy: Simulator-based comparison of two- and three-dimensional transrectal US modalities," *Radiology*, vol. 254, no. 2, pp. 587–594, 2010.
- [2] S. Natarajan *et al.*, "Clinical application of a 3D ultrasound-guided prostate biopsy system," *Urologic Oncol., Seminars Original Invest.*, vol. 29, no. 3, pp. 334–342, 2011.
- [3] P. A. Pinto *et al.*, "Magnetic resonance imaging/ultrasound fusion guided prostate biopsy improves cancer detection following transrectal ultrasound biopsy and correlates with multiparametric magnetic resonance imaging," *J. Urol.*, vol. 186, no. 4, pp. 1281–1285, 2011.
- [4] O. Mohareri *et al.*, "Intraoperative registered transrectal ultrasound guidance for robot-assisted laparoscopic radical prostatectomy," *J. Urol.*, vol. 193, no. 1, pp. 302–312, Jan. 2015.
- [5] M. de Rooij, E. H. J. Hamoen, J. J. Fütterer, J. O. Barentsz, and M. M. Rovers, "Accuracy of multiparametric MRI for prostate cancer detection: A meta-analysis," *Amer. J. Roentgenol.*, vol. 202, no. 2, pp. 343–351, 2014.
- [6] F. Taqee *et al.*, "Deformable prostate registration from MR and TRUS images using surface error driven FEM models," *Proc. SPIE*, vol. 8316, p. 831612, Feb. 2012.
- [7] S. Khallaghi *et al.*, "Statistical biomechanical surface registration: Application to MR-TRUS fusion for prostate interventions," *IEEE Trans. Med. Imag.*, vol. 34, no. 12, pp. 2535–2549, Dec. 2015.
- [8] O. Zetting *et al.*, "Multimodal image-guided prostate fusion biopsy based on automatic deformable registration," *Int. J. Comput. Assist. Radiol. Surgery*, vol. 10, no. 12, pp. 1997–2007, Dec. 2015.
- [9] Y. Sun, J. Yuan, M. Rajchl, W. Qiu, C. Romagnoli, and A. Fenster, "Efficient convex optimization approach to 3D non-rigid MR-TRUS registration," in *Proc. Int. Conf. Med. Image Comput. Comput.-Assist. Intervent.*, 2013, pp. 195–202.
- [10] Y. Hu, E. Gibson, H. U. Ahmed, C. M. Moore, M. Emberton, and D. C. Barratt, "Population-based prediction of subject-specific prostate deformation for MR-to-ultrasound image registration," *Med. Image Anal.*, vol. 26, no. 1, pp. 332–344, Dec. 2015.
- [11] M. Baumann, P. Mozer, V. Daanen, and J. Troccaz, "Prostate biopsy tracking with deformation estimation," *Med. Image Anal.*, vol. 16, no. 3, pp. 562–576, 2012.
- [12] J. Krücker *et al.*, "Fusion of real-time transrectal ultrasound with pre-acquired MRI for multi-modality prostate imaging," *Proc. SPIE*, vol. 6509, p. 650912, Mar. 2007.
- [13] F. Shen, R. Narayanan, and J. S. Suri, "Rapid motion compensation for prostate biopsy using GPU," in *Proc. EMBS*, Aug. 2008, pp. 3257–3260.
- [14] S. Xu *et al.*, "Closed-loop control in fused MR-TRUS image-guided prostate biopsy," in *Proc. MICCAI*, 2007, pp. 128–135.
- [15] S. Khallaghi *et al.*, "A 2D-3D registration framework for freehand TRUS-guided prostate biopsy," in *Proc. MICCAI*, 2015, pp. 272–279.
- [16] S. Y. Selmi, E. Promayon, and J. Troccaz, "3D-2D ultrasound feature-based registration for navigated prostate biopsy: A feasibility study," in *Proc. IEEE 38th Annu. Int. Conf. Eng. Med. Biol. Soc. (EMBC)*, Aug. 2016, pp. 4109–4112.
- [17] D. J. Gillies, L. Gardi, T. De Silva, S.-R. Zhao, and A. Fenster, "Real-time registration of 3D to 2D ultrasound images for image-guided prostate biopsy," *Med. Phys.*, vol. 44, no. 9, pp. 4708–4723, Sep. 2017.
- [18] G. Nir *et al.*, "Model-based registration of *ex vivo* and *in vivo* MRI of the prostate using elastography," *IEEE Trans. Med. Imag.*, vol. 32, no. 6, pp. 1068–1080, Jun. 2013.
- [19] W. J. M. van de Ven, Y. Hu, J. O. Barentsz, N. Karssemeijer, D. Barratt, and H. J. Huisman, "Biomechanical modeling constrained surface-based image registration for prostate MR guided TRUS biopsy," *Med. Phys.*, vol. 42, no. 5, pp. 2470–2481, May 2015.
- [20] O. Mohareri, G. Nir, J. Lobo, R. Savdie, P. Black, and S. Salcudean, "A system for MR-ultrasound guidance during robot-assisted laparoscopic radical prostatectomy," in *Proc. Int. Conf. Med. Image Comput. Comput.-Assist. Intervent.*, 2015, pp. 497–504.
- [21] W. Qiu, J. Yuan, and A. Fenster, "3D prostate MR-TRUS non-rigid registration using dual optimization with volume-preserving constraint," *Proc. SPIE*, vol. 9784, p. 97841P, Mar. 2016.
- [22] O. Goksel and S. E. Salcudean, "B-mode ultrasound image simulation in deformable 3-D medium," *IEEE Trans. Med. Imag.*, vol. 28, no. 11, pp. 1657–1669, Nov. 2009.
- [23] J. E. Bresenham, "Algorithm for computer control of a digital plotter," *IBM Syst. J.*, vol. 4, no. 1, pp. 25–30, Mar. 1965.
- [24] O. Mohareri, M. Ramezani, T. K. Adebar, P. Abolmaesumi, and S. E. Salcudean, "Automatic localization of the da Vinci surgical instrument tips in 3-D transrectal ultrasound," *IEEE Trans. Biomed. Eng.*, vol. 60, no. 9, pp. 2663–2672, Sep. 2013.
- [25] O. Goksel, K. Sapchuk, W. J. Morris, and S. E. Salcudean, "Prostate brachytherapy training with simulated ultrasound and fluoroscopy images," *IEEE Trans. Biomed. Eng.*, vol. 60, no. 4, pp. 1002–1012, Apr. 2013.